

ARMY RESEARCH LABORATORY



**Spherical Indentation in Elastoplastic Materials:
Modeling and Simulation**

by John D. Clayton

ARL-TR-3516

May 2005

NOTICES

Disclaimers

The findings in this report are not to be construed as an official Department of the Army position unless so designated by other authorized documents.

Citation of manufacturer's or trade names does not constitute an official endorsement or approval of the use thereof.

DESTRUCTION NOTICE—Destroy this report when it is no longer needed. Do not return it to the originator.

Army Research Laboratory

Aberdeen Proving Ground, MD 21005-5069

ARL-TR-3516

May 2005

**Spherical Indentation in Elastoplastic Materials:
Modeling and Simulation**

John D. Clayton

Weapons and Materials Research Directorate, ARL

REPORT DOCUMENTATION PAGE

Form Approved
OMB No. 0704-0188

Public reporting burden for this collection of information is estimated to average 1 hour per response, including the time for reviewing instructions, searching existing data sources, gathering and maintaining the data needed, and completing and reviewing the collection information. Send comments regarding this burden estimate or any other aspect of this collection of information, including suggestions for reducing the burden, to Department of Defense, Washington Headquarters Services, Directorate for Information Operations and Reports (0704-0188), 1215 Jefferson Davis Highway, Suite 1204, Arlington, VA 22202-4302. Respondents should be aware that notwithstanding any other provision of law, no person shall be subject to any penalty for failing to comply with a collection of information if it does not display a currently valid OMB control number.

PLEASE DO NOT RETURN YOUR FORM TO THE ABOVE ADDRESS.

1. REPORT DATE (DD-MM-YYYY) May 2005		2. REPORT TYPE Final		3. DATES COVERED (From - To)	
4. TITLE AND SUBTITLE Spherical Indentation in Elastoplastic Materials: Modeling and Simulation				5a. CONTRACT NUMBER	
				5b. GRANT NUMBER	
				5c. PROGRAM ELEMENT NUMBER	
6. AUTHOR(S) John D. Clayton (ARL)				5d. PROJECT NUMBER 1L1622618AH80	
				5e. TASK NUMBER	
				5f. WORK UNIT NUMBER	
7. PERFORMING ORGANIZATION NAME(S) AND ADDRESS(ES) U.S. Army Research Laboratory Weapons and Materials Research Directorate Aberdeen Proving Ground, MD 21005-5069				8. PERFORMING ORGANIZATION REPORT NUMBER ARL-TR-3516	
9. SPONSORING/MONITORING AGENCY NAME(S) AND ADDRESS(ES)				10. SPONSOR/MONITOR'S ACRONYM(S)	
				11. SPONSOR/MONITOR'S REPORT NUMBER(S)	
12. DISTRIBUTION/AVAILABILITY STATEMENT Approved for public release; distribution is unlimited.					
13. SUPPLEMENTARY NOTES					
14. ABSTRACT An implicit axisymmetric finite element model is implemented to study the response of an elastoplastic substrate in contact with a rigid spherical indenter. A finite strain, rate-independent, isotropic elastic-plastic constitutive formulation is invoked for the behavior of the substrate. Relative influences on the load displacement response of elastic stiffness constants and plastic properties of the substrate are investigated via a series of simulations. With increasing depth of indentation, the flow stress overtakes the elastic modulus as the dominant mechanical property with regard to the extracted mechanical response. In agreement with theoretical predictions, Poisson's ratio exerts a very minor effect on the load displacement curves, with this effect further diminishing upon yielding of the substrate at greater depths of indentation. Numerical results are compared with experimental load displacement data for pure metals, alloys, and composite microstructures comprised of titanium, tungsten, tin, and/or polymeric nylon. Relatively close agreement between experiment and simulation is achieved over the loading phase of the indentation cycle for exclusively metallic substrates. Comparatively less success is attained in matching numerical and experimental results for materials of polymeric composition, presumably because of the effects of anisotropy, strain rate dependence (e.g., viscosity) and/or heterogeneities at the microstructural level not captured by the constitutive theory used in the simulations.					
15. SUBJECT TERMS elastoplastic; finite element model; indentation; substrate					
16. SECURITY CLASSIFICATION OF:			17. LIMITATION OF ABSTRACT SAR	18. NUMBER OF PAGES 30	19a. NAME OF RESPONSIBLE PERSON John D. Clayton
a. REPORT Unclassified	b. ABSTRACT Unclassified	c. THIS PAGE Unclassified			19b. TELEPHONE NUMBER (Include area code) 410-306-0975

Contents

List of Figures	iv
List of Tables	iv
Acknowledgments	v
1. Introduction	1
2. Model	2
2.1 Constitutive Formulation.....	2
2.2 Problem Setup	3
3. Preliminary Simulations	5
4. Experiments and Simulations: A Comparison of Results	9
4.1 Ti-6Al-4V Alloy.....	9
4.2 W-Sn Alloys.....	11
4.3 W-Nylon Blends.....	12
5. Conclusions and Recommendations	14
6. References	16
Appendix A. ABAQUS Input Deck	19
Distribution List	22

List of Figures

Figure 1. Initial (a), intermediate (b), and final (c) indenter positions.	3
Figure 2. Finite element mesh, 4900 elements.	4
Figure 3. Elastic and plastic mechanical properties for Ti-6Al-4V.	5
Figure 4. Stress $\bar{\sigma}$ [Pa] in (a) deformed intermediate and (b) unloaded final configurations, $R = 25 \mu\text{m}$, $d = 2 \mu\text{m}$ (frictionless contact, with $u^r(r = W) = 0$, 4900 element mesh).	6
Figure 5. Indentation force P versus displacement δ , effects of mesh densities and far-field boundary conditions.	6
Figure 6. Indentation force P versus displacement δ , effects of indenter radius and friction coefficient, $d = 2 \mu\text{m}$	7
Figure 7. Force versus displacement, effects of Young's modulus E for $R = 25 \mu\text{m}$: (a) $d = 5 \mu\text{m}$, (b) $d = 0.05 \mu\text{m}$	8
Figure 8. Indentation force P versus displacement δ , effects of Poisson's ratio ν for $R = 25$ μm : (a) $d = 5 \mu\text{m}$, (b) $d = 0.05 \mu\text{m}$	8
Figure 9. Indentation force P versus displacement δ , effects of flow stress for $R = 25 \mu\text{m}$ and $d = 5 \mu\text{m}$	9
Figure 10. Indentation force P versus displacement δ , Ti-6Al-4V, experiment and simulation.	10
Figure 11. Experimental, simulated, and analytical elastic uniaxial stress-strain responses.	11
Figure 12. Indentation force P versus displacement δ for (a) W-Sn alloy 70K32 and (b) W-Sn alloy K4754.	12
Figure 13. Indentation force P versus displacement δ for W-nylon materials (a) RVV4B, (b) O26QX, and (c) 1AA63.	13

List of Tables

Table 1. Material parameters obtained experimentally and verified by indentation simulation.	15
--	----

Acknowledgments

The author would like to thank the following people:

From the U.S. Army Research Laboratory, Mark VanLandingham is acknowledged for conducting physical indentation experiments and providing the corresponding load-versus-depth data cited in this report. Daniel Casem is recognized for providing experimental tensile stress-strain data on polycrystalline Ti-6Al-4V. Paul Moy and Tusit Weerasooriya are thanked for sharing experimental yield stress values for W-Sn and W-Nylon materials. Helpful technical suggestions from Mark VanLandingham, Thomas Juliano, Stephan Bilyk, and Edward Rapacki are noted.

From the Massachusetts Institute of Technology, Krystyn Van Vliet also provided helpful suggestions.

INTENTIONALLY LEFT BLANK

1. Introduction

Instrumented indentation techniques enable characterization of the mechanical response of small material samples over wide ranges of spatial resolution and deformation magnitude via choice of size and shape of indenters and depth of indentation. Indentation methods have been used to study, for example, dislocation accumulation and strain gradient effects in ductile metals (Nix & Gao, 1998), lattice friction resistance to dislocation mobility in body-centered cubic crystals (Qiu et al., 2001), fracture processes in ceramics (Clarke & Tandon, 1995), and the mechanical behavior of thin films (Saha & Nix, 2002; Gerberich et al., 2003). The underlying theory used to derive mechanical properties from indentation data (Oliver & Pharr, 1992; Hay et al., 1999) has historically been based upon isothermal, rate-independent elastic or elastic-plastic constitutive assumptions—the latter extending to the inelastic response of the original solution of Hertz (1896) of elastic contact between parabolic solids of revolution. In recent years, VanLandingham and coworkers (VanLandingham et al., 2001; VanLandingham, 2003) have developed a dynamic indentation method exploiting frequency response characteristics of the substrate material in order to probe time-dependent constitutive behavior at large time scales (e.g., viscoelasticity and creep). This method involves a superimposition of high frequency, small amplitude loadings with a single quasi-static cycle of larger magnitude. Experimental techniques exploiting moiré interferometry (Lu et al., 2003) have likewise been developed for elucidating viscous effects at small time scales (e.g., high rate dynamic plasticity).

Numerical simulations based on finite element analysis provide opportune support for the process of development of physically realistic constitutive models, and the acquisition of necessary material parameters for these models via matching of simulated indentation responses with force displacement data acquired from physical experiments (Bhattacharya & Nix, 1988). Typically, numerical indentation studies are conducted to acquire elastic moduli, hardness values, and less commonly in plastic materials, the static yield point and strain hardening exponent (Dao et al., 2001; Chollacoop et al., 2003). Hill and coworkers (Hill et al., 1989) performed a detailed theoretical and numerical study of the Brinell hardness test (i.e., indentation by a spherical ball) applied to elastic-plastic media. Vaidyanathan et al. (2001) used a combined experimental-numerical approach to characterize pressure-sensitive yield in a metallic glass. Methods have also been developed for reproducing entire uniaxial stress-strain curves purely from spherical indentation load displacement data (Herbert et al., 2001), although these are presently regarded by the scientific community as rough estimates at best.

In the present work, we study the response of elastic-plastic materials subjected to spherical indentation. Section 2 describes the problem setup, specifically an axisymmetric finite element model of a rigid indenter contacting a thick, homogeneous slab of substrate material. A finite strain, rate-independent, isotropic elastic-plastic constitutive formulation is invoked for the

behavior of the substrate. In section 3, the relative effects of selected simulation parameters are investigated, including mesh geometry, elastic stiffness constants, and plastic properties. A titanium alloy (Ti-6Al-4V) was chosen as the default substrate material in this parametric investigation. In section 4, we compare results of numerical simulations with experimental load displacement data for alloyed and polymeric blends comprised of tungsten (W), tin (Sn), and/or nylon. Conclusions and recommendations follow in section 5.

2. Model

2.1 Constitutive Formulation

The finite element model consists of a rigid spherical indenter and elastoplastic substrate. The mechanical response of the substrate is dictated by classical, rate-independent, isotropic elastoplasticity theory. Only minimal aspects of this theory are given here; for additional details, the reader may consult the literature (Hill, 1950; Marin & McDowell, 1996). Hereafter, vectors and tensors of rank 2 and above are written in bold face type, and scalars are written in italics.

The kinematic description is based on an additive decomposition of the velocity gradient \mathbf{L} , an assumption consistent with the multiplicative decomposition of Lee (1969) only when the condition of small elastic stretch is applicable:

$$\mathbf{L} = \frac{\partial \mathbf{v}}{\partial \mathbf{x}} = \mathbf{D} + \mathbf{W} = \mathbf{D}^e + \mathbf{D}^p + \mathbf{W}, \quad (1)$$

in which \mathbf{x} are spatial coordinates, $\mathbf{v} = \dot{\mathbf{x}}$ with the superposed dot a material time derivative, the spin $2\mathbf{W} = \mathbf{L} - \mathbf{L}^T$ with the superposed T denoting the transposition, and \mathbf{D}^e and \mathbf{D}^p the elastic and plastic deformation rates, respectively. Following the introduction of suitable co-rotational measures, the strain rate decomposition may be written in time-integrated form via the transformation

$$\mathbf{D} = \mathbf{D}^e + \mathbf{D}^p \rightarrow \boldsymbol{\varepsilon} = \boldsymbol{\varepsilon}^e + \boldsymbol{\varepsilon}^p, \quad (2)$$

where the elastic ($\boldsymbol{\varepsilon}^e$) and plastic ($\boldsymbol{\varepsilon}^p$) strain tensors sum to the total integrated strain measure $\boldsymbol{\varepsilon}$, the latter equivalent to the symmetric part of the spatial displacement gradient only in the limit of small strains and rotations. The isotropic elastic response is described by

$$\boldsymbol{\sigma}' = 2G\boldsymbol{\varepsilon}^e, \quad p = -K\varepsilon_v, \quad (3)$$

where $\boldsymbol{\sigma}' = \boldsymbol{\sigma} + p\mathbf{1}$ is the Cauchy stress deviator, $p = -(1/3)tr(\boldsymbol{\sigma})$ is the hydrostatic pressure, $\boldsymbol{\varepsilon}^e = \boldsymbol{\varepsilon} - (1/3)\varepsilon_v\mathbf{1}$, and $\varepsilon_v = tr(\boldsymbol{\varepsilon})$, assuming isochoric plastic deformation. The identity tensor

is written here as **1**. Shear modulus G , bulk modulus K , Young's modulus E , and Poisson's ratio ν are interrelated via

$$2G(1+\nu) = 3K(1-2\nu) = E. \quad (4)$$

The flow rule for plastic strain increment $d\boldsymbol{\varepsilon}^p$ over time sub-step Δt is written

$$d\boldsymbol{\varepsilon}^p = \dot{e}^p \mathbf{n}^p \Delta t, \quad (5)$$

in which \dot{e}^p is the scalar effective plastic strain rate and the direction of flow is coaxial with the deviatoric stress, i.e.,

$$\mathbf{n}^p = \frac{3}{2\bar{\sigma}} \boldsymbol{\sigma}', \quad (6)$$

with the effective stress $2\bar{\sigma}^2 = 3\boldsymbol{\sigma}' : \boldsymbol{\sigma}'$. The plastic strain rate is determined by consistency with the yield condition

$$\bar{\sigma} = \sigma_y(e^p), \quad (7)$$

where the yield stress σ_y is chosen here as a simple monotonic function of the cumulative effective plastic strain $e^p = \int \dot{e}^p dt$.

2.2 Problem Setup

Finite element analyses were conducted with the ABAQUS¹/Implicit (2002) commercial package, with the preceding constitutive formulation available in the software's standard material library. All analyses were isothermal and quasi-static (i.e., inertial forces were neglected). As shown in figure 1, the boundary value problem exhibits an axisymmetric geometry in the $r-z$ plane. The indenter radius is labeled R , and W and H denote the substrate dimensions. The initial configuration is shown in figure 1(a). During the simulation history, the indenter is depressed in the $-z$ -direction a distance d into the substrate (figure 1(b)), and then returned along the reverse path to its initial position (figure 1(c)). The force acting on the indenter, directed in the $-z$ -direction, is labeled P .

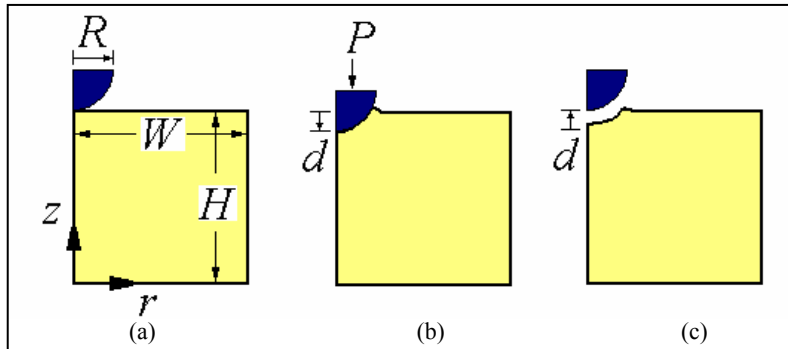


Figure 1. Initial (a), intermediate (b), and final (c) indenter positions.

¹ABAQUS is not an acronym.

The indenter was modeled as an analytical rigid surface, while the deformable substrate was discretized into four-node quadrilateral (axisymmetric) elements featuring reduced integration and “hourglass” control. Boundary conditions on the substrate were specified by

$$\begin{aligned}
 u^r = u^z = 0 & \quad (\text{along } z = 0) \\
 u^r = 0 & \quad (\text{along } r = 0) \\
 t^z = \sigma^{rz} n_r = 0 & \quad (\text{along } r = W) \\
 \left. \begin{aligned}
 t^z = \sigma^{zz} n_z = 0 \\
 t^r = \sigma^{rz} n_z = 0
 \end{aligned} \right\} & \quad (\text{along contact-free portion of } z = H)
 \end{aligned} \tag{8}$$

in which \mathbf{u} is the displacement field, \mathbf{t} is the traction vector per current configuration area, and \mathbf{n} is the unit normal vector to the surface of the body. Preliminary simulations were conducted in order to investigate effects of indenter and substrate dimensions, finite element mesh densities, contact friction, and elastoplastic properties, as discussed in the next section. Various boundary conditions were investigated for the far-field edge defined by $r = W$, also discussed in section 3. A typical mesh is shown in figure 2, here consisting of 4900 elements. Notice that the mesh density is deliberately highest in the vicinity of the contact region beneath the tip of indenter.

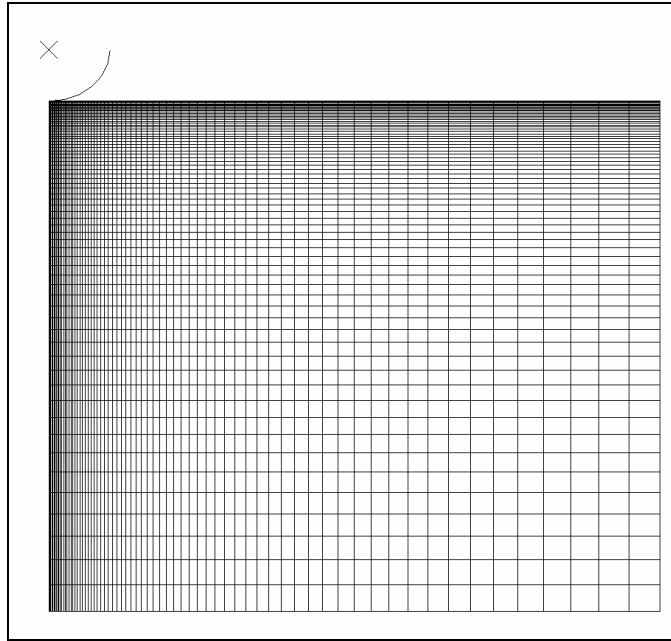


Figure 2. Finite element mesh, 4900 elements.

3. Preliminary Simulations

The default material of study in the preliminary simulations was Ti-6Al-4V, a ductile alloy featuring a polycrystalline hexagonal closely packed (HCP) microstructure. The elastic constants E and ν and effective deviatoric yield stress $\bar{\sigma} = \sigma_y(e^p)$ for this material are given in figure 3, obtained, respectively, from wave speed and mass density measurements and a uniaxial quasi-static tension test, with $\bar{\epsilon}$ the logarithmic strain (see Burkins et al., 2001). Note that $\bar{\sigma}$ is equivalent to the measured true stress in a uniaxial stress state. In the simulations, the elastic constants and post-yielding stress-strain behavior were specified as separate input data (see appendix A).

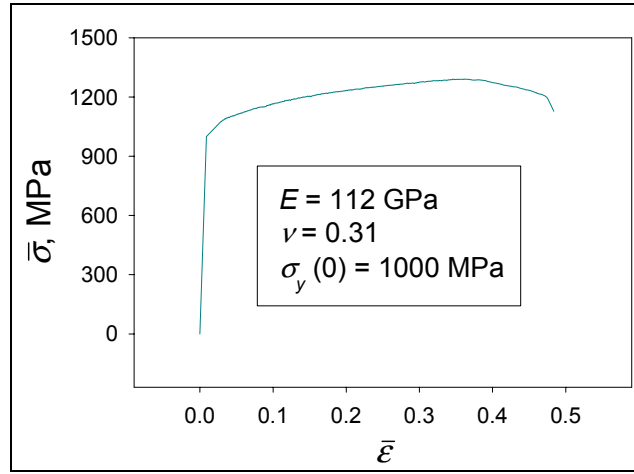


Figure 3. Elastic and plastic mechanical properties for Ti-6Al-4V.

Figure 4 shows the effective deviatoric stress in the substrate, in the loaded and unloaded configurations corresponding to figure 1(b) and 1(c), respectively. Notice that while the stress field is supported by several hundred elements, the response does not spread to the lower and right-most edges of the mesh, along $z = 0$ and $r = W$, respectively. Contours in figure 4(a) correspond to the peak load applied to the indenter, while those in figure 4(b) denote residual stresses remaining in the substrate upon full contact release.

Figure 5 depicts the total force acting on the rigid indenter in the $-z$ -direction, P , versus the total displacement of the indenter in the $-z$ -direction, δ , for various mesh densities and far-field boundary conditions. In the simulations, $\delta \rightarrow d$ during the loading phase, and then $\delta \rightarrow 0$ during unloading. Note that such P versus δ data is our key result acquired from the simulations, as it is used extensively later to compare experimental and simulated findings. In figure 5, “fixed edge” denotes the displacement condition $u^r(r = W) = 0$, while “free edge” denotes the traction condition $t^r(r = W) = 0$. From figure 5, we conclude that the choice of far-field boundary condition has a

negligible effect on the measured P - δ response; thus, the condition $u'(r = W) = 0$ was used exclusively in all other calculations reported here. Analogously, specification of $u' = 0$ along the base of the substrate (along $z = 0$) was deemed appropriate (as opposed to a null shear stress boundary condition), as the stress field did not interact with this boundary in the present simulations. Note that approximately 20 elements at the surface are in direct contact with the indenter in figure 4(a). Furthermore, while 2500 elements appear to offer sufficient resolution, the 4900-element mesh was used in all subsequent calculations, taking advantage of short execution times for the analyses (<900 seconds on a single R14000 Silicon Graphics, Incorporated, processor for the 4900-element mesh upon indentation to $d = 5 \mu\text{m}$).

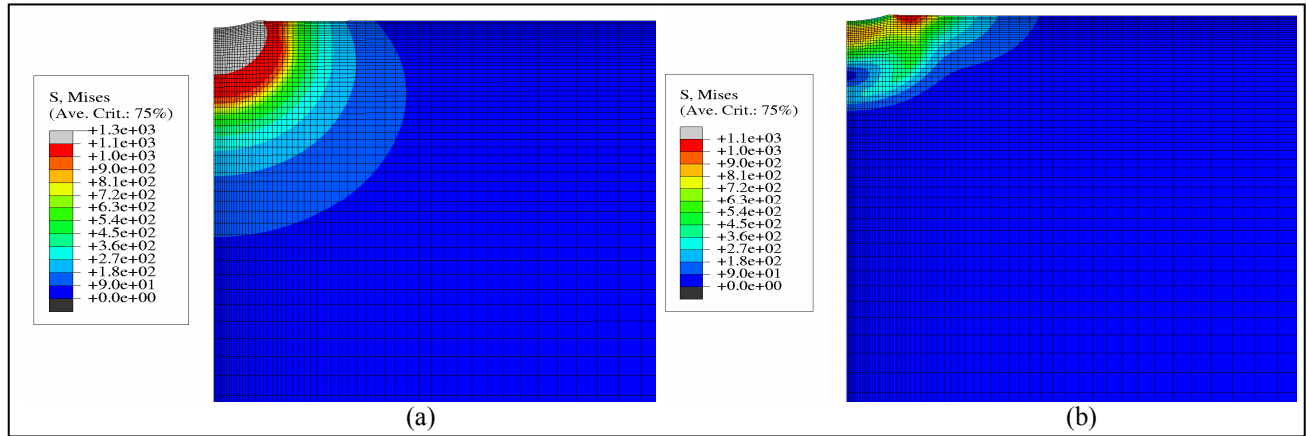


Figure 4. Stress $\bar{\sigma}$ [Pa] in (a) deformed intermediate and (b) unloaded final configurations, $R = 25 \mu\text{m}$, $d = 2 \mu\text{m}$ (frictionless contact, with $u'[r = W] = 0$, 4900-element mesh).

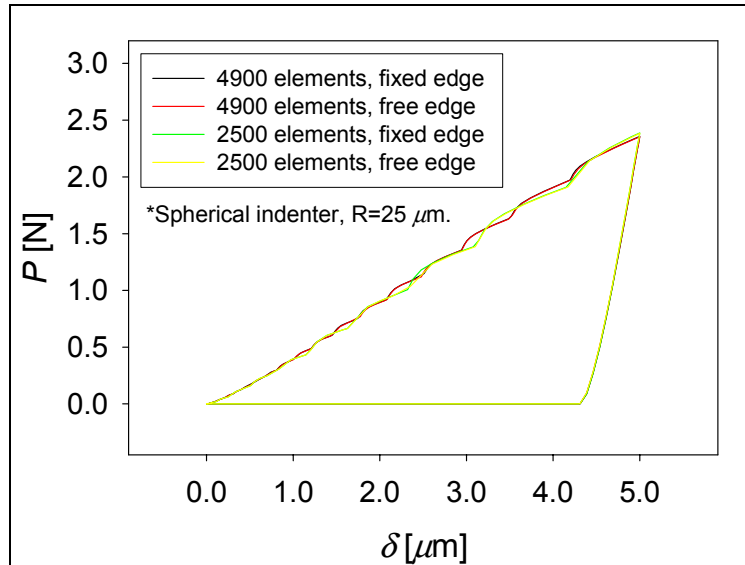


Figure 5. Indentation force P versus displacement δ , effects of mesh densities and far-field boundary conditions.

Figure 6 illustrates effects of indenter radius R and coulomb friction coefficient $\mu = \tau/p$, in which τ is the resultant shear stress opposing relative tangential motion of two surfaces sharing contact pressure p . The geometry of the indenter clearly imposes a dramatic effect on the P - δ response, which is an important consideration when one is matching simulated and experimental data, given the small size of the experimental apparatus whose tip shape and size may not conform precisely to advertised machining specifications. Friction is apparently less important, at least in the context of our simulations, which assume an infinitely rigid indenter. For this reason, and since frictionless contact is the norm in other numerical studies reported in the literature (Bhattacharya & Nix, 1988; Dao et al., 2001; Vaidyanathan et al., 2001; Chollacoop et al., 2003), $\mu = 0$ is invoked in all remaining simulations of the present work.

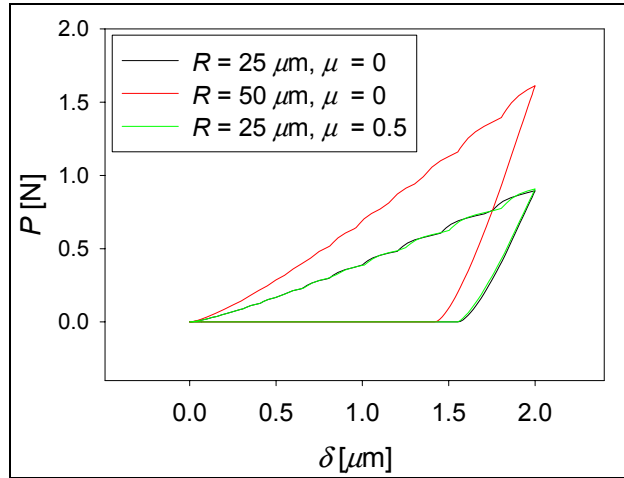


Figure 6. Indentation force P versus displacement δ , effects of indenter radius and friction coefficient, $d = 2 \mu\text{m}$.

Figures 7 and 8 delineate the effects of elastic constants E and ν , respectively, on the computed P - δ response. For simulations corresponding to figures 7(a) and 8(a), the final indentation depth $d = 5 \mu\text{m}$ instills significant yielding and finite plastic deformation in the indentation region, while for simulations corresponding to figures 7(b) and 8(b), the relatively shallow final depth of $d = 0.05 \mu\text{m}$ induces little or no plastic flow, with the presence and degree of yielding depending on the choice of elastic constants. In the simulations associated with figures 7 and 8, all material parameters (e.g., flow stress versus plastic strain) corresponded to those of the actual Ti-6Al-4V material of figure 3, except for the elastic constants that were varied parametrically as indicated in the figure legends (in the legends, $\sigma_y = \sigma_y [e^p = 0] = 1000 \text{ MPa}$). From figure 7, we notice the strong effect of E on the unloading portion of each P - δ curve. From figure 8, the indentation load increases slightly in conjunction with decreasing compressibility of the material (i.e., with increasing ν). When we compare figures 7 and 8, Poisson's ratio appears to exert a lesser effect on the response than Young's modulus, in agreement with analytical theory (Oliver & Pharr, 1992). Furthermore, the effects of elastic constants decrease with increasing indentation depth, as inelastic mechanisms increasingly dominate the response.

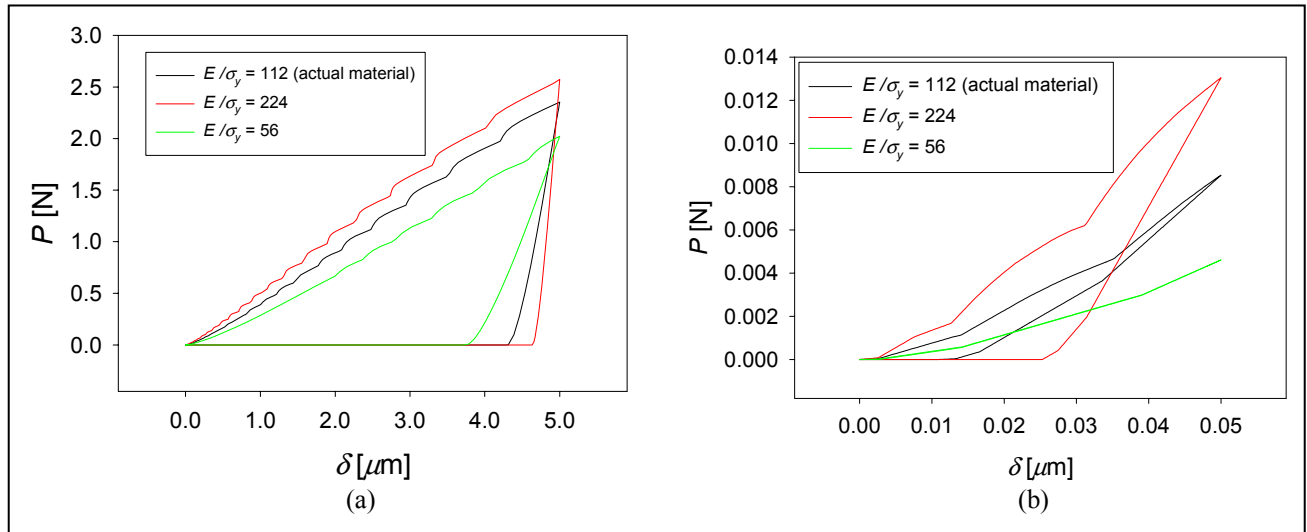


Figure 7. Force versus displacement, effects of Young's modulus E for $R = 25 \mu\text{m}$: (a) $d = 5 \mu\text{m}$, (b) $d = 0.05 \mu\text{m}$.

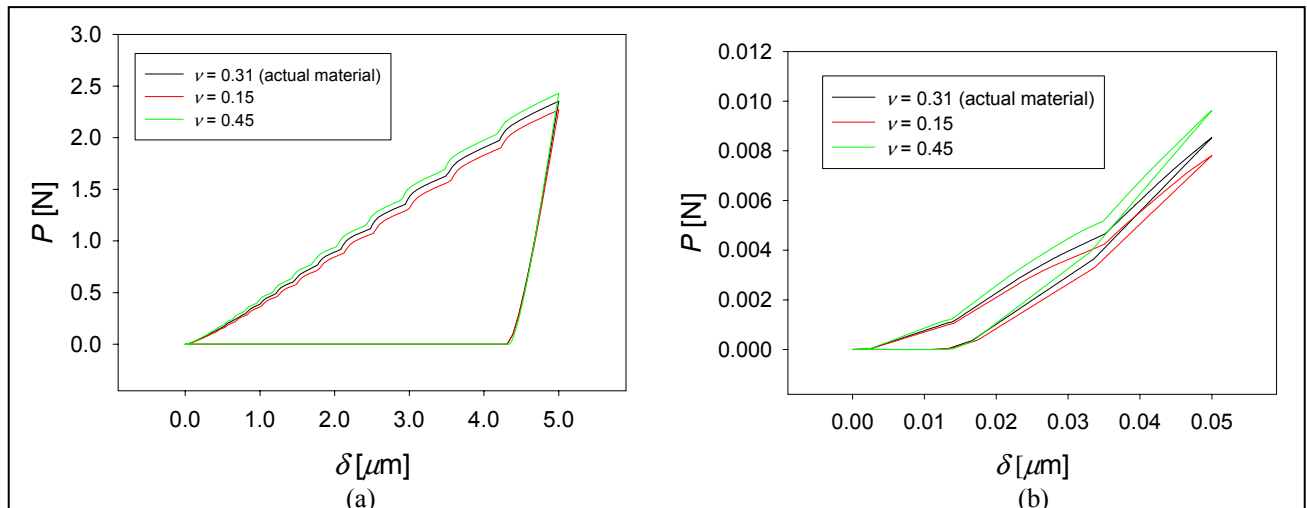


Figure 8. Indentation force P versus displacement δ , effects of Poisson's ratio ν for $R = 25 \mu\text{m}$: (a) $d = 5 \mu\text{m}$, (b) $d = 0.05 \mu\text{m}$.

Figure 9 shows the effect of yield strength on the P - δ response. Two data sets are presented, corresponding to the actual titanium alloy of figure 3 (black curve), and a hypothetical material with the same elastic properties as the former but with a flow stress reduced by 50% (red curve). We compare figures 7(a) and 9, a 50% reduction in flow stress seems to exert much more significant effect on the indentation force measured during the loading phase of the simulation than does a 50% reduction in Young's modulus. On the other hand, the substrate material's flow stress apparently imposes a negligible effect upon the force measured during the unloading portion of the cycle.

Notice also from figures 7 through 9 the fairly jagged nature of the load versus displacement curves, particularly at shallow indentation depths. This phenomenon is not attributable to the

discreteness of the data, since each curve in each figure is comprised of hundreds of data points. Instead, it is thought to be a result of the discreteness of the indenter geometry, constructed of a series of line segments in the finite element model. The jaggedness was not alleviated upon mesh refinement, the use of “full integration” as opposed to “reduced integration” elements, or variation of the hourglass stiffness parameter used in reduced integration elements to suppress excessive distortion. A second cause could be the presence of numerical instabilities in the implicit calculations (e.g., loss of positive-definite tangent stiffness because of relatively weak strain hardening prescribed in the constitutive model).

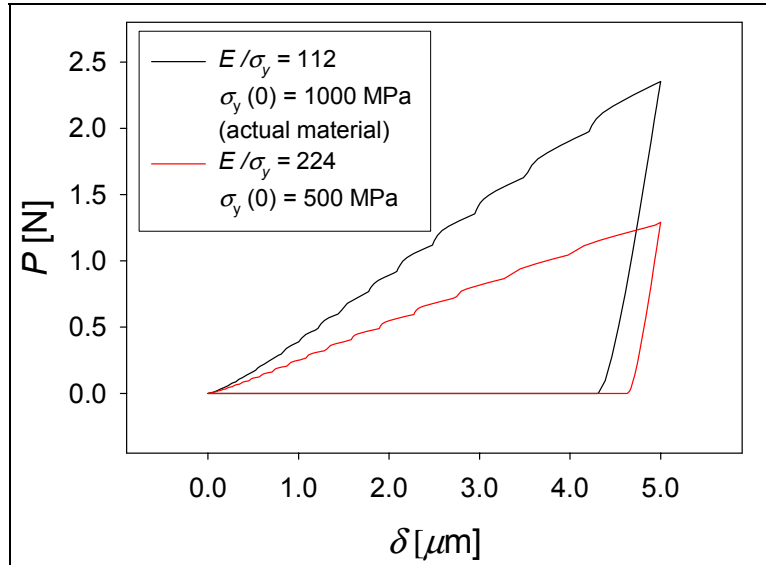


Figure 9. Indentation force P versus displacement δ , effects of flow stress for $R = 25 \mu\text{m}$ and $d = 5 \mu\text{m}$ and.

4. Experiments and Simulations: A Comparison of Results

4.1 Ti-6Al-4V Alloy

Simulated and experimentally obtained results are compared for the Ti-6Al-4V alloy over a range of indentation depths in figure 10. Physical experiments were conducted via the instrumented indentation technique of VanLandingham (2003), featuring a diamond-tipped spherical indenter (radius $R = 25 \mu\text{m}$) undergoing small dynamic oscillations superposed upon the macroscopic load-unload cycle. From figure 10, the P - δ curves agree well during the loading phase; however, the simulations exhibit a noticeably stiffer response upon unloading than do the experiments. This discrepancy may be attributed to elastic and/or plastic anisotropy: the constitutive model used in the simulations is isotropic, while Ti-6Al-4V is a hexagonal microstructure exhibiting an anisotropic tangent stiffness at the single crystal level (cf. Schoenfeld & Kad, 2002). Furthermore, local effects of microstructural heterogeneity at the scale of the contact region (e.g., grain and phase

boundaries, dislocation “pile-ups” or substructure) are not explicitly captured by the classical plasticity model nor are directional strain history effects (e.g., kinematic hardening because of stress directionality under non-monotonic, multi-axial deformation modes). The former effects (i.e., heterogeneity of microstructure) are thought to be of relatively low importance here, even though the grain size is on the order of the indenter size, since experimental repeatability was deemed satisfactory. Finally, the experimental input data for Ti-6Al-4V were acquired from a uniaxial tension test (figure 3), while the indentation experiment produces a primarily compressive stress state. Thus, discrepancies could be caused by tension-compression asymmetry of the material response. Note that the overshoot of the experimental curves by the simulation curves during the loading phase does not indicate a deficiency in predictive capability of the model but merely a differently specified final indentation depth d than that attained in the experiment.

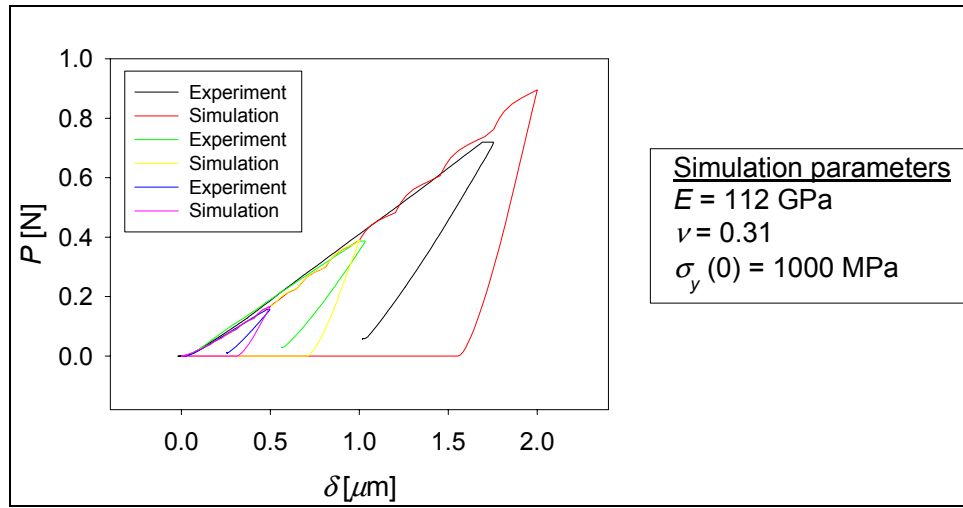


Figure 10. Indentation force P versus displacement δ , Ti-6Al-4V, experiment and simulation.

Figure 11 (red curve) shows the stress-strain prediction reproduced from results of a simulation, conducted with the material properties given in figure 3, with these input parameters corresponding to the black curve in figure 11. The prediction (red curve) is based on the analytical model of Herbert et al. (2001), wherein the equivalent true stress $\bar{\sigma}$ and strain $\bar{\epsilon}$ are defined as

$$\bar{\sigma} = \frac{P}{\pi a^2} = \frac{P}{\pi(2d_c R - d_c^2)}, \quad \bar{\epsilon} = \frac{0.2a}{R} = \frac{0.2\sqrt{2d_c R - d_c^2}}{R}, \quad (9)$$

in which a is the radius of contact and

$$d_c = \delta - \frac{3P}{4S} \quad (10)$$

is the estimated contact depth for a spherical indenter. The elastic contact stiffness S is given by

$$S = 2aE_r, \quad (11)$$

and the reduced elastic modulus is

$$E_r = \left[\frac{1-\nu_i}{E_i} + \frac{1-\nu_s}{E_s} \right]^{-1}, \quad (12)$$

in which E_i and E_s are Young's moduli of the indenter and substrate, respectively, and ν_i and ν_s are Poisson's ratios of the indenter and substrate, respectively. Here, for a rigid indenter, $E_r \rightarrow E_s/(1-\nu_s)$. Given P as a function of δ , equations 9 through 11 are solved iteratively for $\bar{\sigma}$ and $\bar{\epsilon}$. Agreement between original (black) and reproduced (red) curves is considered here to be marginal at best, with the initial yield stress drastically under-predicted at small strains (i.e., for $\bar{\epsilon} < 0.05$). Herbert et al. (2001) reported a similar difficulty in matching uniaxial and indentation data for 6061-T6 aluminum. Also shown in figure 11 is Hertz's elastic solution, in which the force is calculated by

$$P = \frac{4E_r a^3}{3R}, \quad (13)$$

and is then substituted into equations 9 through 11. The elastic response of the material is reproduced quite well by the theory; of course, equation 13 is invalid upon yield, which occurs here at an applied strain of $\bar{\epsilon} = 0.0089$.

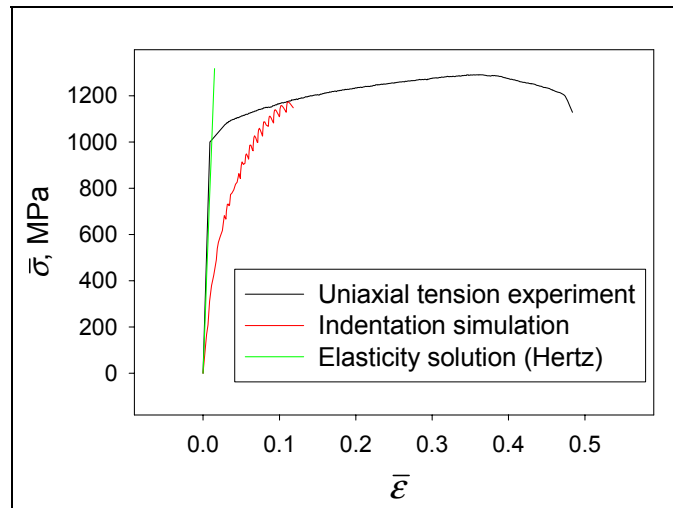


Figure 11. Experimental, simulated, and analytical elastic uniaxial stress-strain responses.

4.2 W-Sn Alloys

The indentation responses of two different W-Sn metallic materials were examined, labeled here as “70K32” and “K4754”. As shown in figure 12, Young's modulus E and/or yield strength σ_y , were varied parametrically in the simulations. Elastic-perfectly plastic behavior was assumed in all cases, as was a fixed Poisson's ratio of $\nu = 0.4$. Insufficient experimental data were available to justify implementation of a more elaborate constitutive model, accounting for strain hardening or viscous effects. Ranges of yield strengths and elastic moduli were chosen on the basis of

values determined by uniaxial tension and instrumented dynamic indentation experiments. For the alloy 70K32 of figure 12(a), it appears that the assumption of constant yield stress (i.e., perfect plasticity) may be inadequate, as the slope of the experimental curve during the loading phase of the indentation cycle increases with depth σ , while the simulated results predict a P - σ response with little curvature. On the other hand, the load displacement response for alloy K4754 of figure 12(b) appears to be well characterized by an elastic-perfectly plastic model. For both W-Sn materials, the elastic modulus E appears to exert little influence on the response relative to the yield strength σ_y at depths greater than several hundred nanometers.

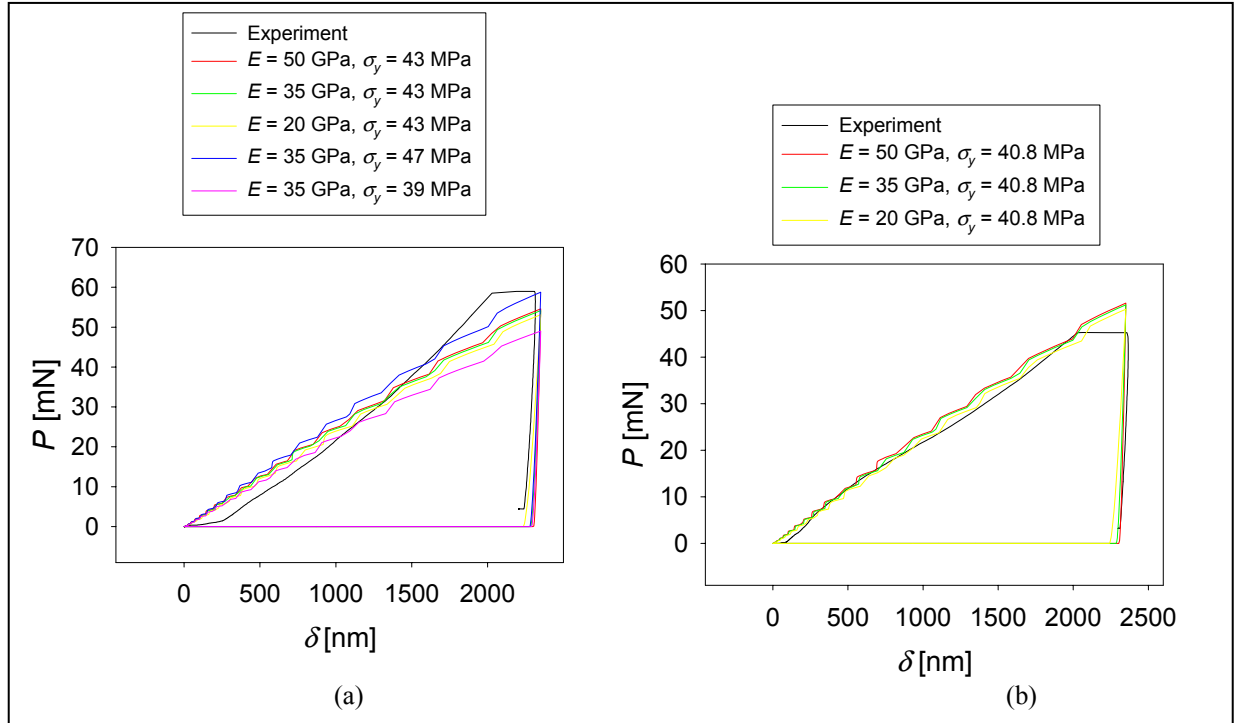


Figure 12. Indentation force P versus displacement δ for (a) W-Sn alloy 70K32 and (b) W-Sn alloy K4754.

4.3 W-Nylon Blends

The indentation responses of three distinct W-Nylon composites were studied, labeled as “RVV4B,” “O26QX,” and “1AA63”. These are high density metal-polymer mixtures. Homogeneous elastic-perfectly plastic behavior was assumed in the simulations of these materials, again with a fixed Poisson’s ratio of $\nu = 0.4$. No composite theory (i.e., properties weighted by volume fractions of W and nylon) was used. As shown in figure 13(a), Young’s modulus E and/or yield strength σ_y were varied parametrically in the simulations of material RVV4B. Ranges of yield strengths and elastic moduli were again chosen based upon values predicted by uniaxial tension tests and instrumented dynamic indentation experiments. Clearly, from figure 13(a), experiment and simulation differ dramatically for all values of simulation parameters. It is hypothesized that the elastic-perfectly plastic model used in these simulations is inadequate because of its inability to capture strain rate effects (i.e., viscoelasticity, time

dependence, and hysteresis) engendered by nylon components of the microstructure. Single simulations were conducted for W-Nylon materials O26QX and 1AA63. Because of the inability of the constitutive model to accurately represent the behavior of these systems, ranges of E and σ_y were not explored for these materials.

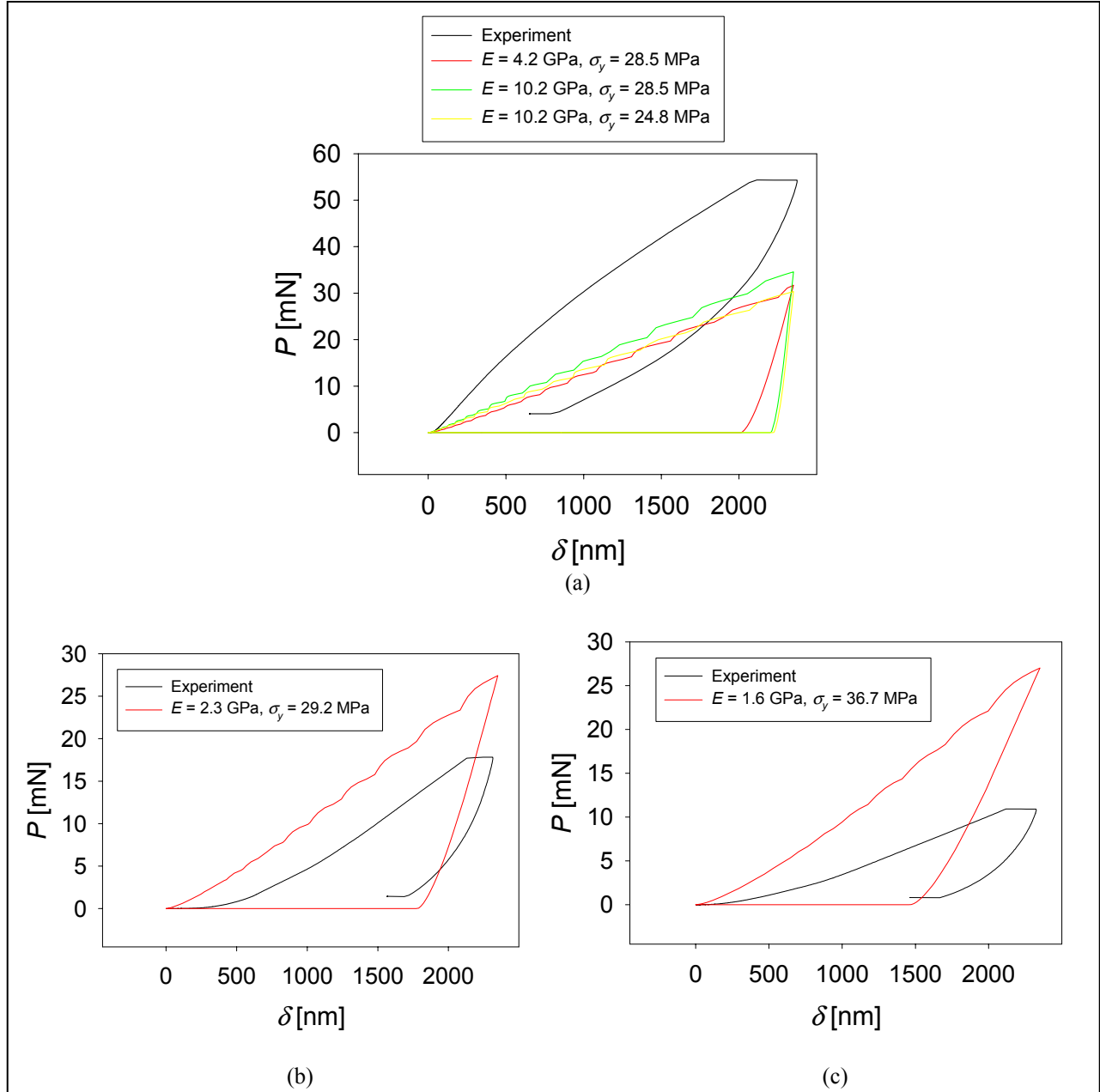


Figure 13. Indentation force P versus displacement δ for W-nylon materials (a) RVV4B, (b) O26QX, and (c) 1AA63.

5. Conclusions and Recommendations

An axisymmetric model of spherical indentation has been developed and invoked within an implicit Lagrangian finite element setting. The model was used to study the load displacement response of elastic-plastic substrates subjected to quasi-static contact with a rigid indenter. The implemented constitutive model assumed rate-independent, isotropic elastic-plastic behavior of the substrate materials. Materials studied included Ti-6Al-4V alloy, W-Sn alloys, and W-Nylon composites. Numerical predictions were compared with results obtained from instrumented indentation experiments. Key findings regarding specific materials include

- Indentation experiment and simulation are capable of close agreement in terms of load displacement response when the constitutive model used in the simulation is accurate with regard to phenomenology and material parameters, as in the case here of a Ti-6Al-4V alloy. For this material, the loading portion of the experimental response was duplicated accurately via finite element simulations, while the elastic unloading portion was not as accurately reproduced. Assumptions of frictionless contact and a rigid indenter did not inhibit simulation accuracy.
- Classical rate-independent, isotropic elastic-plastic constitutive models appear *adequate* for modeling the response of the featured W-Sn materials. The alloy 70K32 appears to undergo strain hardening during indentation, whereas the alloy K4754 appears to exhibit perfectly plastic behavior.
- Classical rate-independent, isotropic elastic-plastic constitutive models appear *inadequate* for modeling the response of the featured W-Nylon materials. These materials seem to exhibit viscoelastic behavior, necessitating an accurate treatment of time-dependent finite elastic deformations.

Table 1 lists material parameters provided by experiment (Young's modulus E from indentation tests; initial yield stress σ_y from uniaxial tension tests) and choices of these parameters that enabled simulations to best match the experimental indentation data. Properties prescribed with relative confidence are limited to yield strengths for the W-Sn materials, highlighted in yellow. The present set of simulations did not permit accurate prescription of properties for the W-Nylon materials; however, the simulations did permit us to substantiate the inadequacy of rate-independent metal plasticity constitutive models for describing their mechanical behavior. Also shown for comparison purposes are the ideal properties used for the Ti-6Al-4V material used to validate the computational approach.

Table 1. Material parameters obtained experimentally and verified by indentation simulation.

Material Identifier	Composition	E (GPa)		σ_y (MPa)	
		Experiment	Simulation	Experiment	Simulation
70K32	Tungsten-Tin	35 ± 15	35	43 ± 3.6	46.6
K4754	Tungsten-Tin	35 ± 15	35	40.8 ± 7.4	40.8
RVV4B	Tungsten-Nylon	4.2 ± 6	--	28.5 ± 3.7	--
O26QX	Tungsten-Nylon	2.3 ± 3	--	29.2 ± 4.4	--
1AA63	Tungsten-Nylon	1.6 ± 2	--	36.7 ± 4.3	--
Ti-6Al-4V	Titanium-Aluminum- Vanadium	112	112	1000	1000

In summary, for homogeneous isotropic elastic-plastic substrate materials exhibiting small elastic strains (e.g., most conventional polycrystalline metals), coupled experimental and numerical indentation methods

- Appear to enable verification of Young’s modulus measurements for elastic (shallow) indentation.
- Appear to enable verification of yield strength measurements for plastic (deep) indentation.
- Do not appear to enable verification of Poisson’s ratio, unless Young’s modulus is known precisely.
- Appear to enable one to detect the presence of and estimate the degree of inelastic strain hardening.

In future studies of metals, it may be worthwhile to implement crystal-plasticity-based formulations (cf. Schoenfeld & Kad, 2002) accounting for anisotropic elastic and inelastic responses engendered by local crystallographic orientation, since the contact region for micron-sized diameters will typically be confined to surface areas spanning one or a few crystals in typical engineering metals with grain sizes on the order of tens of microns. Analogously, more descriptive constitutive theories for polymers may also offer closer agreement between simulation and experiment (e.g., models capturing finite anisotropic viscoelastic effects) (cf. Kaliske, 2000). Note that at even finer scales of spatial resolution, microstructural heterogeneities in the form of dislocations, grain and phase boundaries, and point defects may exert considerable influence on the response, especially for nanoscopic indenter dimensions. In such situations, continuum mechanics treatments may be merged with atomic physics in order to resolve the effects of individual lattice defects, for example, in coupled atomistic-continuum schemes such as the quasi-continuum method (Tadmor et al., 1996; Shenoy et al., 1999) or atomistically informed fully finite element methods (Zhu et al., 2004).

6. References

- ABAQUS, 2002. Version 6.3.5, Hibbitt, Karlsson, and Sorensen, Inc., Pawtucket, RI.
- Bhattacharya, A. K.; Nix, W. D. Finite element simulation of indentation experiments. *Int. J. Solids Structures* **1988**, *24*, 881-891.
- Burkins, M.; Wells, M.; Fanning, J.; Roopchand, B. *The mechanical and ballistic properties of an electron beam single melt of Ti-6Al-4V plate*; ARL-MR-515; , 2001.
- Chollacoop, N.; Dao, M.; Suresh, S. Depth-sensing instrumented indentation with dual sharp indenters. *Acta Mater.* **2003**, *51*, 3713-3729.
- Clarke, D. R.; Tandon, R. Factors affecting the fracture resistance of silicon-nitride ceramics. *Mat. Sci. Eng.* **1995**, *A195*, 207-214.
- Dao, M.; Chollacoop, N.; Van Vliet, K. J.; Venkatesh, T. A.; Suresh, S. Computational modeling of the forward and reverse problems in instrumented sharp indentation. *Acta Mater.* **2001**, *49*, 3899-3918.
- Gerberich, W. W.; Jungk, J. M.; Li, M.; Volinsky, A. A.; Hoehn, J. W.; Yoder, K. Length scales for the fracture of nanostructures. *Int. J. Fracture* **2003**, *119/120*, 387-405.
- Hay, J. C.; Bolshakov, A.; Pharr, G. M. A critical examination of the fundamental relations used in the analysis of indentation data. *J. Mater. Res.* **1999**, *14*, 2296-2305.
- Herbert, E. G.; Pharr, G. M.; Oliver, W. C.; Lucas, B. N.; Hay, J. C. On the measurement of stress-strain curves by spherical indentation. *Thin Solid Films* **2001**, 398-399, 331-335.
- Hertz, H. In: H. Hertz (Ed.), *Miscellaneous Papers*; Eds. Jones and Schott, Macmillan, London, 1896.
- Hill, R. *The Mathematical Theory of Plasticity*; Oxford University Press, London, 1950.
- Hill, R.; Storåkers, B.; Zdunek, A. B. A theoretical study of the Brinell hardness test. *Proc. R. Soc. Lond.* **1989**, *A423*, 301-330.
- Kaliske, M. A formulation of elasticity and viscoelasticity for fibre reinforced material at small and finite strains. *Comp. Meth. Appl. Mech. Engng.* **2000**, *185*, 225-243.
- Lee, E. H. Elastic-plastic deformations at finite strains. *J. Appl. Mech.* **1969**, *36*, 1-6.
- Lu, J.; Suresh, S.; Ravichandran, G. Dynamic indentation for determining the strain rate sensitivity of metals. *J. Mech. Phys. Solids* **2003**, *51*, 1923-1938.

- Marin, E. B.; McDowell, D. L. Associative versus non-associative porous viscoplasticity based on internal state variable concepts. *Int. J. Plasticity* **1996**, *12*, 629-669.
- Nix, W. D.; Gao, H. Indentation size effects in crystalline materials: a law for strain gradient plasticity. *J. Mech. Phys. Solids* **1998**, *46*, 411-425.
- Oliver, W. C.; Pharr, G. M. An improved technique for determining hardness and elastic modulus using load and displacement sensing indentation experiments. *J. Mater. Res.* **1992**, *7*, 1564-1583.
- Qiu, X.; Huang, Y.; Nix, W. D.; Hwang, K. C.; Gao, H. Effect of intrinsic lattice resistance in strain gradient plasticity. *Acta Mater.* **2001**, *49*, 3949-3958.
- Saha, R.; Nix, W. D. Effects of the substrate on the determination of thin film mechanical properties by nanoindentation. *Acta Mater.* **2002**, *50*, 23-38.
- Schoenfeld, S. E.; Kad, B. Texture effects on shear response in Ti-6Al-4V plates. *Int. J. Plasticity* **2002**, *18*, 461-486.
- Shenoy, V. B.; Miller, R.; Tadmor, E. B.; Rodney, D.; Phillips, R.; Ortiz, M. An adaptive finite element approach to atomic-scale mechanics-the quasicontinuum method. *J. Mech. Phys. Solids* **1999**, *47*, 611-642.
- Tadmor, E. B.; Ortiz, M.; Phillips, R. Quasicontinuum analysis of defects in solids. *Phil. Mag.* **1996**, *A 73*, 1529-1563.
- Vaidyanathan, R.; Dao, M.; Ravichandran, G.; Suresh, S. Study of mechanical deformation in bulk metallic glass through instrumented indentation. *Acta Mater.* **2001**, *49*, 3781-3789.
- VanLandingham, M. Review of instrumented indentation. *J. Res. Natl. Inst. Stand. Technol.* **2003**, *108*, 249-265.
- VanLandingham, M. R.; Villarrubia, J. S.; Guthrie, W. F.; Meyers, G. F. *Macromol. Symp.* **2001**, *167*, 15.
- Zhu, T.; Li, J.; Van Vliet, K. J.; Ogata, S.; Yip, S.; Suresh, S. Predictive modeling of nanoindentation induced homogeneous defect nucleation in copper. *J. Mech. Phys. Solids* **2004**, *52*, 691-724.

INTENTIONALLY LEFT BLANK

Appendix A. ABAQUS Input Deck

An ABAQUS input deck is given below for quasi-static indentation and release of a slab of Ti-6Al-4V material, with an indenter radius of $25\ \mu\text{m}$, to an indentation depth of $5\ \mu\text{m}$. The software used for the present work was version 6.3-5 (2002).

```
*HEADING
  STATIC INDENTATION WITH A HEMISPHERICAL PUNCH
*****
**  Measure the punch reaction force during the following 2 steps:
**    Step 1: Displace punch 1R units downwards.
**    Step 2: Return punch to original position.
**          (Force Units: N, MPa, mm, sec)
**  R is the unit radius of the punch.
**  Mesh is 10R x 10R, 1/5 suggested by Hill et al., Pr. Roy. Soc., 1989
**  4900 elements, 5041 nodes for target material
*****
*PREPRINT,MODEL=YES,HISTORY=NO
*RESTART,WRITE
*NODE
1, 0.,250.
71, 250.,250.
4971, 0.,0.
5041,250.,0.
*NSET,NSET=N1
1,
*NSET,NSET=N71
71,
*NSET,NSET=N4971
4971,
*NSET,NSET=N5041
5041,
*NFILL,NSET=TOP,BIAS=0.95
N1,N71,70,1
*NFILL,NSET=BOT,BIAS=0.95
N4971,N5041,70,1
*NFILL,NSET=ALLN,BIAS=0.95
TOP,BOT,70,71
*NSET,NSET=CENTER,GENERATE
1,4971,71
*NSET,NSET=OUTSIDE,GENERATE
71,5041,71
*ELEMENT,TYPE=CAX4R
1,72,73,2,1
*ELGEN,ELSET=SUBSTRATE
1,70,1,1,70,71,70
*ELSET,ELSET=CENT,GENERATE
1,4901,70
*ELSET,ELSET=ETOP,GENERATE
1,70,1
```

```

*NODE,NSET=PUNCH
100000,0.,275.
*SOLID SECTION,ELSET=SUBSTRATE,MATERIAL=TIAL
*HOURGLASS STIFFNESS
213.4
*****
*MATERIAL,NAME=TIAL
*ELASTIC
112000,0.31
*PLASTIC,HARDENING=ISOTROPIC
1000,0.0
1075.9739,0.0201
1099.8646,0.0324
1125.0435,0.0526
1150.9742,0.0793
1175.6331,0.1024
1200.0284,0.1344
1225.2135,0.1738
1250.0531,0.2272
1275.4083,0.2908
1290.6458,0.3369
*****
*BOUNDARY
BOT,1,2
CENTER,1
100000,1
100000,6
OUTSIDE,1
*****
*SURFACE,TYPE=SEGMENTS,NAME=IMPACTOR
START,25.,275.
CIRCL,0.,250.,0.,275.
*SURFACE,TYPE=ELEMENT,NAME=TARGET
ETOP,S3
*RIGID BODY,ANALYTICALSURFACE=IMPACTOR,REFNODE=100000
*CONTACT PAIR,INTERACTION=ROUGH
TARGET,IMPACTOR
*SURFACE INTERACTION,NAME=ROUGH
*FRICTION
0.0,
*****
*STEP,NLGEOM,INC=200,AMPLITUDE=RAMP,UNSYMM=YES
Displace punch XR units downwards.
*STATIC
.0015,1.,,.05
*BOUNDARY
100000,2,2,-5
*PRINT,CONTACT=YES
*CONTACT CONTROLS,FRICTION ONSET=DELAY
*CONTACT PRINT,SLAVE=TARGET
**CONTACT FILE,SLAVE=TARGET,FREQUENCY=10
*EL PRINT,FREQUENCY=50,ELSET=CENT
S,
E,
*NODE PRINT,FREQUENCY=1
U,
RF,

```

```

*OUTPUT, FIELD, FREQUENCY=1
*NODE OUTPUT
  U, V, A, RF
*ELEMENT OUTPUT
  S, LE, NE
*CONTACT OUTPUT, VARIABLE=PRESELECT, NSET=TOP
*OUTPUT, HISTORY, FREQUENCY=1
*NODE OUTPUT, NSET=PUNCH
  U, V, A, RF
*ELEMENT OUTPUT, ELSET=CENT
  S, LE, NE
*END STEP
*****
*STEP, NLGEOM, INC=200, AMPLITUDE=RAMP, UNSYMM=YES
  Return punch to original position.
*STATIC
.0015, 1., .015
*BOUNDARY, OP=MOD
100000, 2, 2, 0.0
*OUTPUT, FIELD, FREQUENCY=1
*NODE OUTPUT
  U, V, A, RF
*ELEMENT OUTPUT
  S, LE, NE
*CONTACT OUTPUT, VARIABLE=PRESELECT, NSET=TOP
*OUTPUT, HISTORY, FREQUENCY=1
*NODE OUTPUT, NSET=PUNCH
  U, V, A, RF
*ELEMENT OUTPUT, ELSET=CENT
  S, LE, NE
*ENERGY OUTPUT, VARIABLE=PRESELECT
*END STEP

```

NO. OF
COPIES ORGANIZATION

- * ADMINISTRATOR
DEFENSE TECHNICAL INFO CTR
ATTN DTIC OCA
8725 JOHN J KINGMAN RD STE 0944
FT BELVOIR VA 22060-6218
*pdf file only
- 1 DIRECTOR
US ARMY RSCH LABORATORY
ATTN IMNE ALC IMS MAIL & REC MGMT
2800 POWDER MILL RD
ADELPHI MD 20783-1197
- 1 DIRECTOR
US ARMY RSCH LABORATORY
ATTN AMSRD ARL CI OK TL TECH LIB
2800 POWDER MILL RD
ADELPHI MD 20783-1197
- ABERDEEN PROVING GROUND
- 1 DIRECTOR
US ARMY RSCH LABORATORY
ATTN AMSRD ARL CI OK (TECH LIB)
BLDG 4600
- 1 DIRECTOR
US ARMY RSCH LABORATORY
ATTN AMSRD ARL WM BC J NEWILL
BLDG 390
- 1 DIRECTOR
US ARMY RSCH LABORATORY
ATTN AMSRD ARL WM M S MCKNIGHT
BLDG 4600
- 3 DIRECTOR
US ARMY RSCH LABORATORY
ATTN AMSRD ARL WM MA
M VANLANDINGHAM
T JULIANO P MOY
BLDG 4600
- 1 DIRECTOR
US ARMY RSCH LABORATORY
ATTN AMSRD ARL WM MB J SOUTH
BLDG 4600
- 1 DIRECTOR
US ARMY RSCH LABORATORY
ATTN AMSRD ARL WM TA S SCHOENFELD
BLDG 393

NO. OF
COPIES ORGANIZATION

- 5 DIRECTOR
US ARMY RSCH LABORATORY
ATTN AMSRD ARL WM TD T BJERKE
S BILYK D CASEM E RAPACKI
T WEERASOORIYA
BLDG 4600